Strong super-rotation during the 2018 Martian Global Dust Storm

Kylash Rajendran[1], Stephen R. Lewis[1], James A. Holmes[1], Paul M. Streeter[1], Anna A. Fedorova[2], and Manish R. Patel[1,3]

[1]School of Physical Sciences, The Open University, Milton Keynes, UK
[2]Space Research Institute of the Russian Academy of Sciences (IKI RAS), Moscow, Russia
[3]Space Science and Technology Department, Science and Technology Facilities Council, Rutherford Appleton Laboratory, Oxfordshire, United Kingdom

Key Points:

- Super-rotation in the martian atmosphere was greatly enhanced during the Mars Year 34 Global Dust Storm
- Strengthened tropical winds were instrumental in transporting dust across the globe during the initial stages of the Global Dust Storm
- Tracking of dust plumes using data assimilation yielded estimates of wind speeds in the tropics of 10-15 m/s below 10 km

Corresponding author: Kylash Rajendran, `kylash.rajendran@open.ac.uk`

Abstract

We report on the strong enhancement of tropical winds in the martian atmosphere during the Global Dust Storm of Martian Year 34, as revealed by an assimilation of temperature and dust observations into a martian global climate model. We demonstrate that global super-rotation almost doubled at the peak of the dust storm period, as compared to Mars Year 33, which did not have a Global Dust Storm. The enhanced westerly jet played a key role in the initial stages of the dust storm, transporting dust across the planet and between different lifting centers. By tracking the progression of dust plumes, we derive estimates of wind speeds in the lower tropical atmosphere of 10-15 m/s below 10 km. The tropical region was dominated by diurnal and semi-diurnal tides, with a significant amplification of the gravest Kelvin mode during the onset of the storm.

Plain Language Summary

Dust plays a major role in driving the behaviour of the atmosphere of Mars. During a Global Dust Storm, winds lift and transport dust throughout the atmosphere; in turn, dust affects wind direction and strength by heating and cooling the surrounding air. Using a technique that allowed us to combine satellite observations with simulations of the martian atmosphere, we demonstrate that winds at tropical latitudes were greatly strengthened during the 2018 martian Global Dust Storm as a result of heating by dust. We show that these winds played a crucial role in transporting dust across the globe during the initial stages of the storm. By tracking the locations of the observed dust plumes, we were able to estimate wind speeds in the lower atmosphere of Mars.

1 Introduction

A planetary atmosphere is said to be in a state of *super-rotation* if the total axial angular momentum of the atmosphere is greater than the angular momentum of an atmosphere in a state of pure solid body rotation (Read, 1986). Super-rotation usually takes the form of a prograde equatorial zonal jet, and it has been shown that such a state must be maintained by the equatorward transport of angular momentum by non-axisymmetric eddy motions (Hide, 1969). Identifying the exact mechanisms that initiate and maintain super-rotating jets remains a significant challenge in planetary atmospheric research, and is crucial for understanding the atmospheric dynamics of slow-rotating terrestrial planets such as Venus and Titan (Read & Lebonnois, 2018). The martian atmosphere is also a candidate for super-rotation, as first identified by Lewis and Read (2003).

Global Dust Storms (GDS) are planetary-scale dust lifting events in the martian atmosphere that occur every few martian years, and are the most dramatic of all the dust-driven atmospheric phenomena on the planet. During a GDS, large parts of the planet are enveloped in a shroud of dust that can persist for several months at a time, drastically affecting the atmospheric state. Such storms have all been observed to occur during the high dust loading season (L_S=180°−360°), when the planet's orbit brings it closer to the Sun. The most recent GDS occurred in Mars Year (MY) 34 (using the naming convention of Clancy et al. (2000)). The storm initiated shortly after the northern hemisphere autumn equinox at L_S=187°, and its evolution was monitored by multiple orbital, surface and Earth-based instruments (Guzewich et al., 2019; Kass et al., 2019; Smith, 2019; Sánchez-Lavega et al., 2019; Felici et al., 2019; Jain et al., 2020; Aoki et al., 2019; Stcherbinine et al., 2020).

The formation mechanisms of a GDS are still not well understood; in particular, it has not been established why a GDS forms out of regional storms in some years, but not others. Posited hypotheses include the re-distribution of dust between finite reservoirs between years (Mulholland et al., 2013; Newman & Richardson, 2015), and a weak coupling between orbital and rotational angular momentum on Mars (Shirley, 2017; Newman et al., 2019).

Lewis and Read (2003) have shown that dust-driven heating can excite a super-rotating jet in the martian atmosphere. In dusty conditions (such as during a GDS), the enhanced absorption of solar and thermal radiation amplifies the thermal tides, which are normal modes of the atmospheric response to diurnal solar forcing. The westward propagation of these tides away from their tropical source regions then enables an eastward super-rotating jet to form.

One might expect that a strengthening of the equatorial jet by the presence of dust would also affect dust transport, at least in the tropical regions where the jet is strongest. Transport of dust by the jet determines the locations of further dust-driven heating; in this way, there is an intimate link between dust-driven heating and the strength of the equatorial jet which may have implications for GDS evolution.

In this paper, we investigate dust-driven super-rotation of the martian atmosphere during the MY 34 GDS, using a data assimilation scheme (Lewis et al., 2007) to assimilate temperature and dust data from the Mars Climate Sounder (MCS) and Atmospheric Chemistry Suite (ACS) instruments into a Mars Global Climate Model (MGCM). We show that the atmosphere was strongly super-rotating during the dust storm period, driven by excited thermal tides. The enhanced equatorial jet is shown to play a significant role in transporting dust eastwards during the initial phases of the storm, and we estimate the strength of zonal winds by tracking the eastward migration of dust plumes.

In Section 2, we describe the model and assimilation scheme that we used for this study, and we briefly describe the observational datasets utilised in the assimilation. We also describe some super-rotation metrics that will be used later in the study. Results are presented in Section 3, and we discuss our findings in Section 4.

2 Data and Methods

2.1 Observation data

MCS is a passive 9-channel limb-scanning radiometer aboard the Mars Reconnaissance Orbiter (MRO) (McCleese et al., 2007). Measurements are taken at approximately 3 am and 3 pm local time along a Sun-synchronous orbit, across a wavelength range of $0.3-45\,\mu$m. Radiance profiles were generated from the surface to around 80 km with an intrinsic vertical resolution of 5 km, enabling the retrieval of profiles of temperature, dust and water ice (Kleinböhl et al., 2009, 2017). For this assimilation study we made use of the temperature observations and derived column dust values from MCS (Montabone et al., 2015), which were available for the duration of MYs 33 and 34.

ACS (Korablev et al., 2018) is an array of three infrared spectrometers aboard the ExoMars Trace Gas Orbiter (TGO), that together provide spectral coverage over a wavelength range of $0.7-17\,\mu$m. The near-infrared (NIR) channel uses an echelle grating with an Acousto-Optical Tunable filter with a resolving power of 25,000, to retrieve atmospheric density and temperature profiles based on the $1.57\,\mu$m CO_2 band (Fedorova et al., 2020). The orbit of TGO allows for solar occultations that cross the terminator over a range of local times, a key feature of these datasets. ACS-NIR temperature profiles were included in our assimilation of MY 34 over the period L_S=163°−360°.

2.2 Global Climate Model and data assimilation scheme

The martian atmosphere is modelled using the UK version of the Laboratoire de Météorologique (LMD) MGCM (Forget et al., 1999). The LMD model contains numerous parameterizations of physical processes on Mars, including schemes for CO_2 condensation and sublimation, radiative transfer, photochemistry, orographic and gravity wave drag, cloud microphysics, convection and the boundary layer (Forget et al., 1999; Lefèvre et al., 2004; Colaïtis et al., 2013; Navarro et al., 2014). Dust transport is via an interactive two-moment scheme that describes the particle size distribution using two tracers, the mass mixing ratio and the number density (Madeleine et al., 2011; Spiga et al., 2013).

The UK-specific variant of the model combines the physics schemes of the LMD model with a spectral dynamical core (Hoskins & Simmons, 1975), a vertical finite difference scheme that conserves energy and angular momentum (Simmons & Burridge, 1981), and a semi-Lagrangian tracer advection scheme (Newman et al., 2002). The model was run at T42 resolution (triangular truncation at horizontal wavenumber 42), which corresponds to a physical grid resolution of 3.75°. 55 unevenly-spaced, terrain-following vertical levels were used, with the model top at approximately 100 km.

The data assimilation scheme is an implementation of the Analysis Correction (AC) scheme, originally developed for terrestrial applications (Lorenc et al., 1991) and later modified and re-tuned for the martian context (Lewis et al., 1996, 2007). The scheme employs a form of successive corrections, with analysis increments interlaced between dynamical timesteps. It has been successfully employed in assimilating profiles of temperature and column dust opacity from the Thermal Emission Spectrometer (TES) (Lewis & Barker, 2005; Montabone et al., 2005; Lewis et al., 2007) and Mars Climate Sounder (MCS) (Steele et al., 2014; Holmes et al., 2019, 2020; Streeter et al., 2020) instruments.

We performed model runs for two consecutive years, MY 33 and MY 34, assimilating spacecraft data into the model where available. Our primary focus is on the dust storm period of MY 34, L_S=180°−240°. The MY 33 assimilation was used for comparison as it was a year that did not have a GDS.

2.3 Super-rotation metrics

Super-rotation can be quantified by defining a global super-rotation index S (Lewis & Read, 2003) as

$$S = \frac{\iiint \rho u a \cos\phi \, dV}{\iiint \rho \Omega a^2 \cos^2\phi \, dV} \times 100\%, \tag{1}$$

where ρ is density, u is the zonal wind velocity, and a, ϕ and Ω are the planetary radius, latitude and rotation rate respectively. The volume element is $dV = a^2 \cos\phi \, d\lambda \, d\phi \, dz$, where λ and z are east longitude and geometric height respectively. Each integral is performed over the whole atmospheric volume. Positive values of S would indicate that the atmosphere as a whole had more angular momentum than if it was in pure solid body rotation.

Alternatively, super-rotation can be diagnosed at a given latitude and height by defining a local super-rotation index s as

$$s = \left[\bar{m}/\Omega a^2 - 1\right] \times 100\%. \tag{2}$$

Here $\bar{m}$ is the zonally averaged value of axial angular momentum m, which is defined as

$$m = a\cos\phi\left[\Omega a \cos\phi + u\right]. \tag{3}$$

s is a local measure of super-rotation, and is essentially a comparison between the zonal-mean angular momentum of a fluid parcel at a given latitude and height, against the angular momentum of an equal-mass parcel at rest at the equator. Positive values of s represent super-rotation.

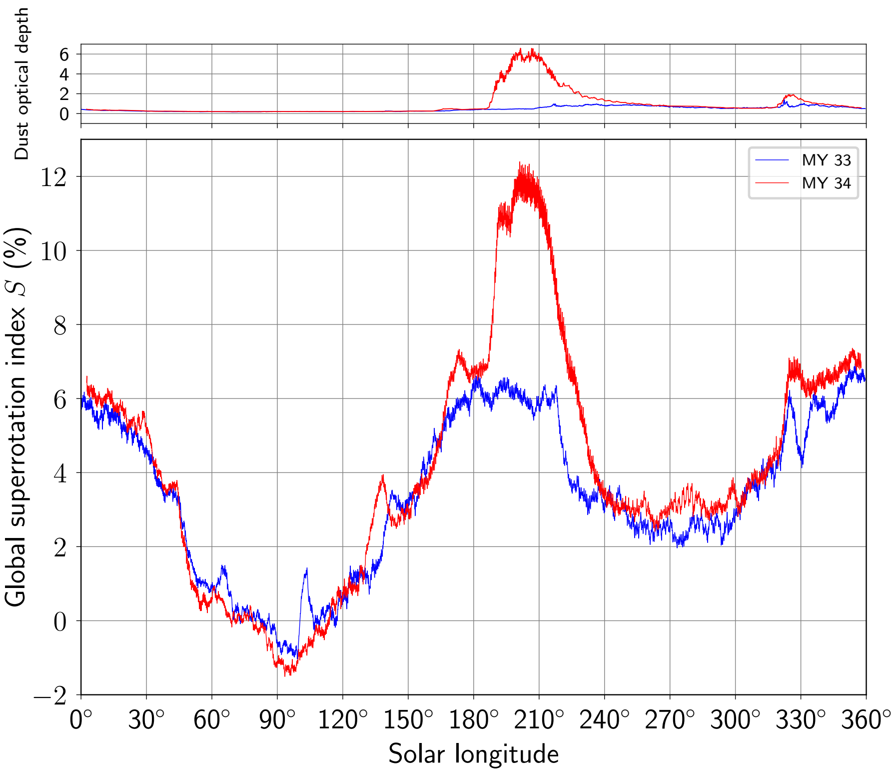

Figure 1. Values of the global super-rotation metric S during MY 33 (blue) and MY 34 (red). Positive values indicate global super-rotation. The upper panel shows the corresponding column dust optical depth values over the equator.

3 Results

3.1 Atmospheric super-rotation

Fig. 1 shows the variation of the global super-rotation metric S through MY 33-34. A major feature in Fig. 1 is the large peak in S centered at L_S=200° in MY 34, which clearly corresponds to the period of the MY 34 GDS. Global super-rotation in MY 34 first diverges significantly from MY 33 values at L_S=165°, when the dust opacity in the tropics first begins to increase. After an initial peak to $S = 7.2\%$ at L_S=173°, global super-rotation increases sharply upon storm onset at L_S=187°, reaching a maximum of $S = 12.6\%$ at L_S=201°. The peak value is twice as large as the corresponding MY 33 value of $S = 6.2\%$, indicating a significant increase in atmospheric angular momentum. After the peak, S decays and returns to background values at L_S=240°.

Outside of the global dust storm period, the values of S are broadly similar in both years. Global super-rotation variations have a semi-annual structure, with broad peaks occurring during equinoxes and troughs occurring during the solstices, due to changes in the Hadley cell structure (Lewis & Read, 2003). S remains largely positive throughout both years of study, except during Northern summer solstice. The average values of S are 3.4% and 3.9% for MY 33 and MY 34 respectively.

Fig. 2 depicts values of zonal-mean zonal winds and the local super-rotation index across latitude and height, during the MY 34 GDS period in both years. The data have

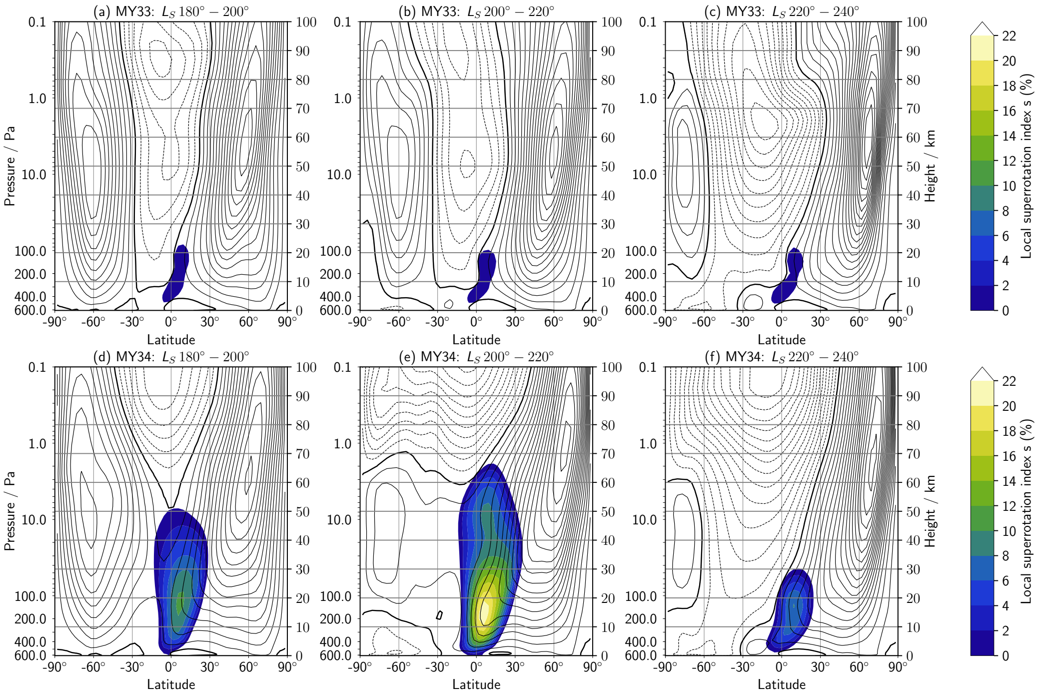

Figure 2. Contours of zonal-mean zonal wind (black) and local super-rotation index (filled, positive values only) during the MY 34 GDS period for MY 33 (top) and MY 34 (bottom). Data in each column is averaged over a solar longitude block of width 20°. Zonal wind contours have been drawn at $10\,\mathrm{m\,s^{-1}}$ intervals, with eastward (westward) winds denoted by solid (dashed) lines. The bold solid contour is the zero wind line.

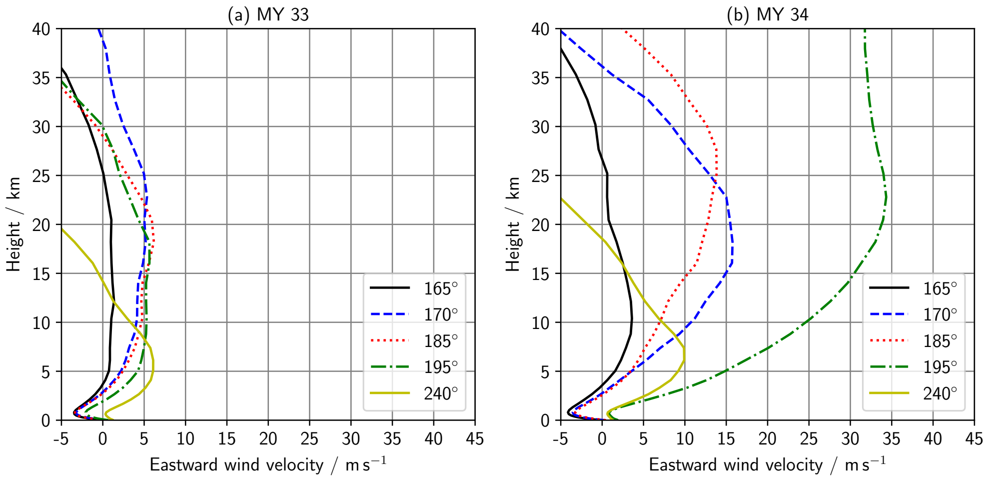

Figure 3. Profiles of zonal-mean zonal wind in the tropics during the MY 34 GDS. Zonal-mean zonal wind has been averaged across the (30° S - 30° N) latitude band, and is displayed at five different solar longitudes for MY 33 (left) and MY 34 (right) respectively.

been averaged in time over 20° periods of solar longitude. These broadly cover the initiation, peak and decay phases of the storm.

In all periods, super-rotation is much stronger in MY 34 than in MY 33. In the time period of storm initiation (Figs. 2(a), 2(d)), the atmosphere is in an equinoctial state, with extratropical westerly jets in both hemispheres and equatorial westerlies. This is reflected by the positive local super-rotation values in the tropics, which a peak of $s \approx 12\%$ at 20 km in MY 34 compared to $s \approx 1\%$ in MY 33.

Super-rotation is strongest in the period $L_S = 200° - 220°$ (Fig. 2(e)), which corresponds to the peak of the dust storm in MY 34. The super-rotating jet continues to dominate the tropical band, and extends up to 60 km. There is a strong peak in local super-rotation in the tropical atmosphere at 20 km, reflecting a significant acceleration of tropical winds by the presence of dust.

In the decay phase of the storm (Fig. 2(f)), easterly winds dominate the tropical regions above 20 km. Super-rotation is greatly reduced in both intensity and extent, and is confined to the lower atmosphere below 30 km.

3.2 Effect of super-rotation on winds and dust transport

Fig. 3 shows zonal-mean zonal wind profiles at four solar longitudes during the initiation phase of the GDS (L_S=165°, 170°, 185°, 195°), and at one solar longitude during the decay phase of the GDS (L_S=240°) for MY 33 (left) and MY 34 (right). Zonal winds have been averaged over the tropical latitude band (30° S–30° N).

The tropical zonal wind profile does not change substantially between L_S=165°–195° of MY 33 (Fig. 3(a)). Easterly winds in the lowermost atmosphere are overlain by westerly winds that peak at 20–25 km with velocities between 5–7 m s^{-1}.

In contrast, enhanced super-rotation has a significant impact on the zonal wind profiles in MY 34. Whilst the wind profile for L_S=165° in MY 34 is similar to the winds in MY 33 discussed above, by L_S=170° zonal wind speeds have increased at almost all heights. The wind profile weakens slightly at L_S=185°, before strengthening substantially to reach

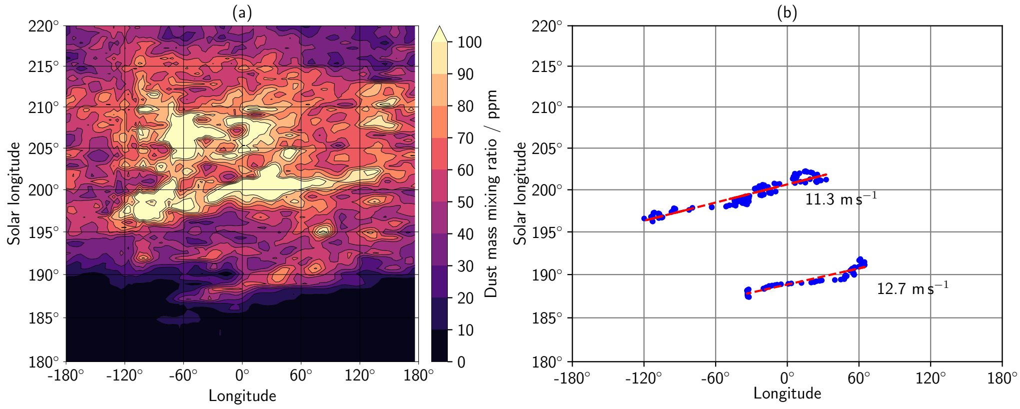

Figure 4. Eastward transport of dust by tropical winds during the MY 34 GDS. (a) Dust mass mixing ratio on the 290 Pa pressure level (≈ 8 km above the surface). Values have been averaged around the equator (10° S−10° N), and are in units of parts per million (ppm). (b) Estimates of zonal wind speed during the initiation phase of the GDS, derived by tracking the mean longitude of the 65 ppm (Chryse plume) and 100 ppm (Tharsis plume) contours.

peak values of 35 m s^{-1} at L_S=195°, with eastward winds penetrating all the way down to the lowest model level (5 m). In the decay phase of the GDS period, wind profiles from MY 34 start to converge with profiles from MY 33.

The enhanced winds in the tropics played a significant role in the transport and distribution of dust during the initial phase of the GDS. Fig. 4(a) shows the evolution of the dust mass mixing ratio, averaged around the equator (10° S−10° N) and plotted on the 290 Pa pressure level (≈ 8 km above the surface). The first signs of enhanced dust presence in the atmosphere appear in Chryse Planitia (40° W, L_S=187°), from which a coherent band of dust can be seen moving eastward from this initial dust excitation region. These winds rapidly transport the dust around the planet, eventually reaching the Tharsis region where a large lifting event is initiated (90° W, L_S=197°). Continued eastward dust transport results in dust being advected back to the original dust lifting region in Chryse.

We obtained indirect estimates of wind speeds on Mars by tracking the eastward propagation rate of the dust plumes. At each model time point and vertical level, a diurnal moving average of the dust mass mixing ratio was calculated, and then averaged across the tropical latitude band. Plots of the 65 ppm and 100 ppm contour lines were constructed across longitude and height, and the mean longitudes of these contour levels were used to estimate the plume locations. The analysis revealed two westward-propagating plumes, shown in Fig. 4(b), with dust propagation speeds of 12.7 m s^{-1} (Chryse plume) and 11.3 m s^{-1} (Tharsis plume). These results are within the range of model wind speeds in the lower atmosphere below 10 km (Fig. 3(b)). We also note that these speeds would not be consistent with model winds below 10 km in the absence of strong dust-driven forcing (Fig. 3(a)), as these winds do not exceed 5 m s^{-1}.

3.3 Tidal excitation during the MY 34 GDS

We performed a Fourier analysis of surface pressure during the GDS period of MY 34. The daily pressure field for each sol was decomposed into the sum of Fourier modes in wavenumber-frequency space.

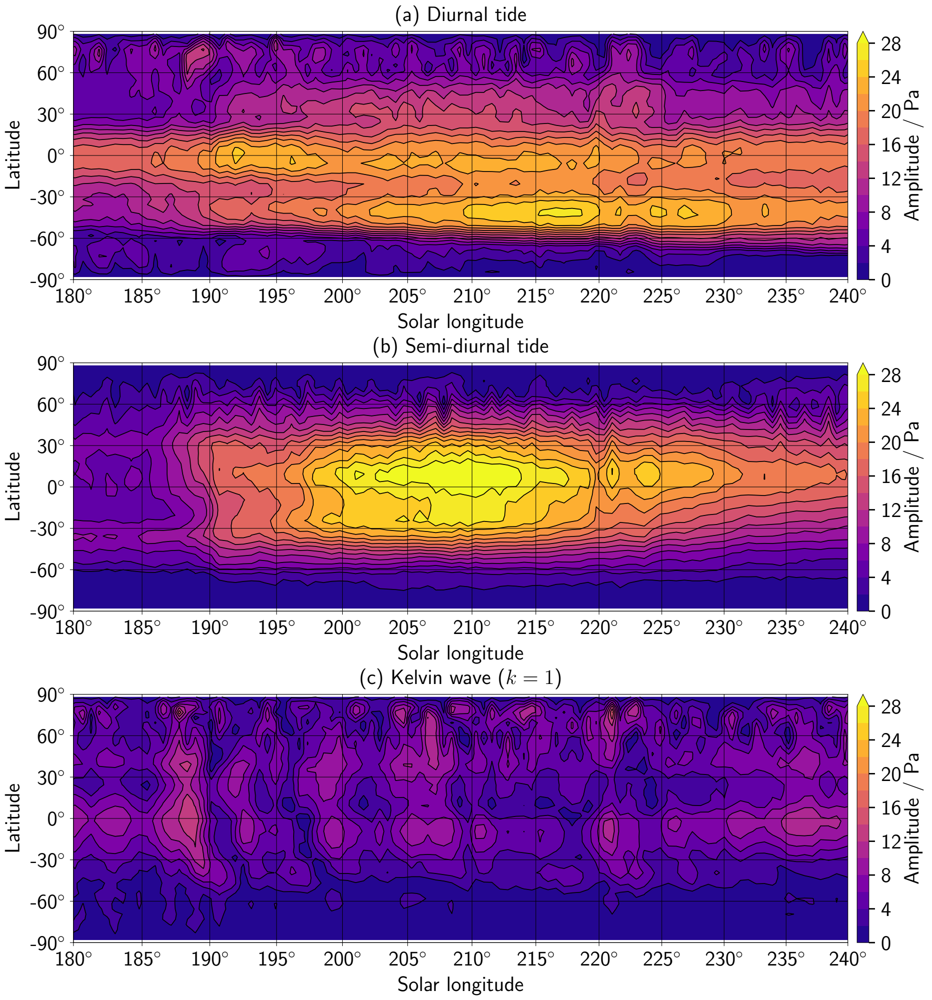

Figure 5. Latitude-time variations of the largest surface pressure modes during the MY 34 GDS: (a) diurnal tide, (b) semi-diurnal tide, and (c) $k = 1$ Kelvin wave.

The modes with the largest amplitudes over the GDS period were the Sun-synchronous diurnal and semi-diurnal tides, which are excited by the diurnal radiative heating and cooling of the atmosphere by solar and thermal radiation. During dusty periods, the increased thermal forcing of the atmosphere results in the enhancement of these modes.

In addition to the tides, the wavenumber-1 Kelvin wave was also found to have significant amplitude. The Kelvin wave is a resonant mode that is excited by the interaction of the diurnal solar heating and the wavenumber-2 variations in topography and thermal inertia on Mars (Zurek, 1976; Wilson & Hamilton, 1996).

Fig. 5 shows the latitudinal variation of these three largest wave modes over the GDS period for MY 34. Amplitudes were generally strongest in the tropical region, and decreased toward the poles.

The diurnal tide was the largest mode during the initiation phase, with an amplitude of 16 Pa (Fig. 5(a)). In comparison, the amplitudes of the other modes were quite weak, with the amplitude of the semi-diurnal tide not exceeding 4 Pa. Upon the onset of dust lifting in the Chryse Planitia region at $L_S = 187°$, the amplitudes of all three modes began to increase. Both the diurnal and semi-diurnal tides experienced a relatively monotonic increase in amplitude with increased dust loading. In contrast, the Kelvin wave response was more varied, increasing dramatically to a peak of 14 Pa at L_S=188°, before decaying rapidly back to background levels of between 2–8 Pa.

As the storm intensified, the amplitude of both sun-synchronous tides increased. Growth of the semi-diurnal tide was more significant due to the essentially linear relationship between the semi-diurnal tide and total dust loading as demonstrated by Lewis and Barker (2005). It eventually surpassed the amplitude of the diurnal tide at the peak of the dust storm, with a value of almost 30 Pa compared to 22 Pa. In the decay phase of the storm, the amplitudes of both modes gradually reduced, with the amplitude of the semi-diurnal tide decreasing faster than the amplitude of the diurnal tide.

4 Discussion

The tropical westerly jet was strongly enhanced during the MY 34 GDS. This had a very large impact on the value of the global super-rotation index S, which doubled in the dust storm period from 6.2% (MY 33) to 12.6% (MY 34). The jet dominated the tropical atmosphere during the peak of the storm, with local super-rotation extending up to 60 km. These changes in tropical wind behaviour had significant consequences for atmospheric tracer transport.

Montabone et al. (2020) reported a value of $S = 16\%$ during the peak of the MY 34 GDS, compared to a pre-dust storm value of 5%. Our results agree qualitatively, and indicate a large increase in super-rotation during the dust storm period. Quantitative differences are likely to be due to the different dynamical cores (spectral versus grid-point) and vertical resolutions (50 versus 29) used by the different models (UK versus LMD).

Transport of dust in the initial phases of the storm was largely controlled by the strength of the westerly tropical jet, which determined the timescale over which dust lofted in Chryse Planitia was transported eastward towards Tharsis. The initial increase in the strength of global super-rotation occurred between L_S=163°–170°, when dust lifted in the southern hemisphere began encroaching into the tropical band. The enhancement of winds occurred quite some time before GDS onset at L_S=187°, and might be an important precursor condition for equinoctial GDS development.

The jet-driven eastward transport of dust back into the Chryse basin from Tharsis during the GDS resulted in a significant rejuvenation of dust activity in that region. This suggests that dust activity in Chryse Planitia may have decayed - and the dust storm not have become global in extent - had the enhanced westerly equatorial jet not been strong enough to transport dust from Tharsis into the Chryse basin.

The propagation of dust plumes in the assimilation was used to estimate wind speeds in the lower martian atmosphere. The plume locations were constrained by satellite-derived observations of the dust distribution, wherever available; at other times, model advection of the dust fields provided self-consistency and improved predictive capabilities at times where observations were unavailable. The self-consistency of these results gives us reason to expect winds on the order of 10-15 m s^{-1} below 10 km during equinoctial global dust storms.

Our results provide strong evidence that a strong super-rotating jet forms in the topics during an equinoctial GDS. This jet has a major role to play in determing the evolution pathway of a GDS, and we have provided estimates of wind speeds in the lowest 10 km of the tropical atmosphere that are consistent with our claims. Future work in this area could explore the dynamics of the super-rotating jet in different GDS years. In addition, the role of the Kelvin wave in the initial phase of the GDS would benefit from further clarification.

Acknowledgments
KR, SRL, JAH and MRP acknowledge the support of the UK Space Agency under the following grants: ST/R00145X/1 (KR, SRL, MRP), ST/S001405/1 (JAH, SRL, MRP), ST/V005332/1 (SRL, MRP) and ST/V002295/1 (MRP). AAF acknowledges the subsidy of the Ministry of Science and Higher Education of the Russian Federation to IKI RAS (theme 'Planeta'). PMS acknowledges the support of the STFC under grant ST/N50421X/1, and the Open University in the form of a PhD studentship. Data from this study may be accessed at `https://figshare.com/s/aa4ee8eab7510d0081dc`.

References

Aoki, S., Vandaele, A., Daerden, F., Villanueva, G., Liuzzi, G., Thomas, I., … others (2019). Water vapor vertical profiles on mars in dust storms observed by tgo/nomad. *J. Geophys. Res.-Planet*, *124*(12), 3482–3497.

Clancy, R., Sandor, B., Wolff, M., Christensen, P., Smith, M., Pearl, J., … Wilson, R. (2000). An intercomparison of ground-based millimeter, mgs tes, and viking atmospheric temperature measurements: Seasonal and interannual variability of temperatures and dust loading in the global mars atmosphere. *J. Geophys. Res.-Planet*, *105*(E4), 9553–9571.

Colaïtis, A., Spiga, A., Hourdin, F., Rio, C., Forget, F., & Millour, E. (2013). A thermal plume model for the martian convective boundary layer. *J. Geophys. Res.-Planet*, *118*(7), 1468–1487.

Fedorova, A., Montmessin, F., Korablev, O., Luginin, M., Trokhimovskiy, A., Belyaev, D., … others (2020). Stormy water on mars: The distribution and saturation of atmospheric water during the dusty season. *Science*, *367*(6475), 297–300.

Felici, M., Withers, P., Smith, M., González-Galindo, F., Oudrhiri, K., & Kahan, D. (2019). Maven rose observations of the response of the martian ionosphere to dust storms. *J. Geophys. Res.-Space*, e2019JA027083.

Forget, F., Hourdin, F., Fournier, R., Hourdin, C., Talagrand, O., Collins, M., … Huot, J. (1999). Improved general circulation models of the martian atmosphere from the surface to above 80 km. *J. Geophys. Res.-Planet*, *104*(E10), 24155–24175.

Guzewich, S., Lemmon, M., Smith, C., Martínez, G., de Vicente-Retortillo, Á., Newman, C., … others (2019). Mars science laboratory observations of the 2018/mars year 34 global dust storm. *Geophys. Res. Lett.*, *46*(1), 71–79.

Hide, R. (1969). Dynamics of the atmospheres of the major planets with an appendix on the viscous boundary layer at the rigid bounding surface of an electrically-conducting rotating fluid in the presence of a magnetic field. *J. Atmos. Sci.*, *26*(5), 841–853.

Holmes, J., Lewis, S., & Patel, M. (2020). Openmars: A global record of martian weather from 1999 2015. *Planet. Space Sci.*, 104962.

Holmes, J., Lewis, S., Patel, M., & Smith, M. (2019). Global analysis and forecasts of carbon monoxide on mars. *Icarus*, *328*, 232–245.

Hoskins, B., & Simmons, A. (1975). A multi-layer spectral model and the semi-implicit method. *Q. J. Roy. Meteo. Soc*, *101*(429), 637–655.

Jain, S., Bougher, S., Deighan, J., Schneider, N., González Galindo, F., Stewart, A., … Pawlowski, D. (2020). Martian thermospheric warming associated with the planet encircling dust event of 2018. *Geophys. Res. Lett.*, *47*(3), e2019GL085302.

Kass, D., Schofield, J., Kleinböhl, A., McCleese, D., Heavens, N., Shirley, J., & Steele, L. (2019). Mars climate sounder observation of mars' 2018 global dust storm. *Geophys. Res. Lett.*.

Kleinböhl, A., Friedson, A., & Schofield, J. (2017). Two-dimensional radiative transfer for the retrieval of limb emission measurements in the martian atmosphere.

J. Quant. Spectrosc. Ra., *187*, 511–522.
Kleinböhl, A., Schofield, J., Kass, D., Abdou, W., Backus, C., Sen, B., … others (2009). Mars climate sounder limb profile retrieval of atmospheric temperature, pressure, and dust and water ice opacity. *J. Geophys. Res.-Planet*, *114*(E10).
Korablev, O., Montmessin, F., Trokhimovskiy, A., Fedorova, A., Shakun, A., Grigoriev, A., … others (2018). The atmospheric chemistry suite (acs) of three spectrometers for the exomars 2016 trace gas orbiter. *Space Sci. Rev.*, *214*(1), 7.
Lefèvre, F., Lebonnois, S., Montmessin, F., & Forget, F. (2004). Three-dimensional modeling of ozone on mars. *J. Geophys. Res.-Planet*, *109*(E7).
Lewis, S., & Barker, P. (2005). Atmospheric tides in a mars general circulation model with data assimilation. *Adv. Space Res.*, *36*(11), 2162–2168.
Lewis, S., & Read, P. (2003). Equatorial jets in the dusty martian atmosphere. *J. Geophys. Res.-Planet*, *108*(E4).
Lewis, S., Read, P., & Collins, M. (1996). Martian atmospheric data assimilation with a simplified general circulation model: Orbiter and lander networks. *Planet. Space Sci.*, *44*(11), 1395–1409.
Lewis, S., Read, P., Conrath, B., Pearl, J., & Smith, M. (2007). Assimilation of thermal emission spectrometer atmospheric data during the mars global surveyor aerobraking period. *Icarus*, *192*(2), 327–347.
Lorenc, A., Bell, R., & Macpherson, B. (1991). The meteorological office analysis correction data assimilation scheme. *Q. J. Roy. Meteo. Soc.*, *117*(497), 59–89.
Madeleine, J., Forget, F., Millour, E., Montabone, L., & Wolff, M. (2011). Revisiting the radiative impact of dust on mars using the lmd global climate model. *J. Geophys. Res.-Planet*, *116*(E11).
McCleese, D., Schofield, J., Taylor, F., Calcutt, S., Foote, M., Kass, D., … Zurek, R. (2007). Mars climate sounder: An investigation of thermal and water vapor structure, dust and condensate distributions in the atmosphere, and energy balance of the polar regions. *J. Geophys. Res.-Planet*, *112*(E5).
Montabone, L., Forget, F., Millour, E., Wilson, R., Lewis, S., Cantor, B., … others (2015). Eight-year climatology of dust optical depth on mars. *Icarus*, *251*, 65–95.
Montabone, L., Lewis, S., & Read, P. (2005). Interannual variability of martian dust storms in assimilation of several years of mars global surveyor observations. *Adv. Space Res.*, *36*(11), 2146–2155.
Montabone, L., Spiga, A., Kass, D., Kleinböhl, A., Forget, F., & Millour, E. (2020). Martian year 34 column dust climatology from mars climate sounder observations: Reconstructed maps and model simulations. *J. Geophys. Res.-Planet*, e2019JE006111.
Mulholland, D., Read, P., & Lewis, S. (2013). Simulating the interannual variability of major dust storms on mars using variable lifting thresholds. *Icarus*, *223*(1), 344–358.
Navarro, T., Madeleine, J., Forget, F., Spiga, A., Millour, E., Montmessin, F., & Määttänen, A. (2014). Global climate modeling of the martian water cycle with improved microphysics and radiatively active water ice clouds. *J. Geophys. Res.-Planet*, *119*(7), 1479–1495.
Newman, C., Lee, C., Mischna, M., Richardson, M., & Shirley, J. (2019). An initial assessment of the impact of postulated orbit-spin coupling on mars dust storm variability in fully interactive dust simulations. *Icarus*, *317*, 649–668.
Newman, C., Lewis, S., Read, P., & Forget, F. (2002). Modeling the martian dust cycle, 1. representations of dust transport processes. *J. Geophys. Res.-Planet*, *107*(E12), 6–1.
Newman, C., & Richardson, M. (2015). The impact of surface dust source exhaustion on the martian dust cycle, dust storms and interannual variability, as

simulated by the marswrf general circulation model. *Icarus*, *257*, 47–87.
Read, P. (1986). Super-rotation and diffusion of axial angular momentum: I.'speed limits' for axisymmetric flow in a rotating cylindrical fluid annulus. *Q. J. Roy. Meteo. Soc.*, *112*(471), 231–251.
Read, P., & Lebonnois, S. (2018). Superrotation on venus, on titan, and elsewhere. *Annu. Rev. Earth Pl. Sc.*, *46*, 175–202.
Sánchez-Lavega, A., del Río-Gaztelurrutia, T., Hernández-Bernal, J., & Delcroix, M. (2019). The onset and growth of the 2018 martian global dust storm. *Geophys. Res. Lett.*, *46*(11), 6101–6108.
Shirley, J. (2017). Orbit-spin coupling and the circulation of the martian atmosphere. *Planet. Space Sci.*, *141*, 1–16.
Simmons, A., & Burridge, D. (1981). An energy and angular-momentum conserving vertical finite-difference scheme and hybrid vertical coordinates. *Mon. Weather Rev.*, *109*(4), 758–766.
Smith, M. (2019). Themis observations of the 2018 mars global dust storm. *J. Geophys. Res.-Planet*, *124*(11), 2929–2944.
Spiga, A., Faure, J., Madeleine, J., Määttänen, A., & Forget, F. (2013). Rocket dust storms and detached dust layers in the martian atmosphere. *J. Geophys. Res.-Planet*, *118*(4), 746–767.
Stcherbinine, A., Vincendon, M., Montmessin, F., Wolff, M., Korablev, O., Fedorova, A., … others (2020). Martian water ice clouds during the 2018 global dust storm as observed by the acs-mir channel onboard the trace gas orbiter. *J. Geophys. Res.-Planet*, *125*(3), e2019JE006300.
Steele, L., Lewis, S., Patel, M., Montmessin, F., Forget, F., & Smith, M. (2014). The seasonal cycle of water vapour on mars from assimilation of thermal emission spectrometer data. *Icarus*, *237*, 97–115.
Streeter, P., Lewis, S., Patel, M., Holmes, J., & Kass, D. (2020). Surface warming during the 2018/mars year 34 global dust storm. *Geophys. Res. Lett.*, *47*(9), e2019GL083936.
Wilson, J., & Hamilton, K. (1996). Comprehensive model simulation of thermal tides in the martian atmosphere. *J. Atmos. Sci.*, *53*(9), 1290–1326.
Zurek, R. (1976). Diurnal tide in the martian atmosphere. *J. Atmos. Sci.*, *33*(2), 321–337.